Ultra-Low-Profile, Electrically Small, Pattern-Reconfigurable Metamaterial-Inspired Huygens Dipole Antenna

Zhentian Wu, Ming-Chun Tang, *Senior Member, IEEE*, Mei Li, *Member, IEEE,* and Richard W. Ziolkowski, *Fellow, IEEE*

Abstract — An ultra-low-profile, electrically small, pattern-reconfigurable metamaterial-inspired Huygens dipole antenna is presented that operates near 1.5 GHz. The design incorporates two pairs of magnetic and electric near-field resonant parasitic (NFRP) elements and a reconfigurable driven element. A pair of p-i-n diodes is integrated into the driven element to enable the antenna pattern reconfigurability. By switching the ON / OFF states of the diodes, the antenna can realize two independent unidirectional endfire radiating states whose peaks point in antipodal directions and a bidirectional endfire radiating state. The measured results, in good agreement with their simulated values, demonstrate that even though the antenna is electrically small ($ka = 0.98$) and ultra-low-profile ($0.0026\lambda_0$), it can realize uniform peak realized gains (RG) ~ 5.4 dBi, front-to-back ratios (FTBR) ~ 13.3 dB, and radiation efficiencies (RE) ~ 85% in its two oppositely directed endfire states, and RG ~ 3.55 dBi and RE ~ 87% in its bidirectional endfire state.

Index Terms—Electrically small antennas (ESAs), Huygens dipole antennas, ultra-low-profile antennas, metamaterial-inspired antennas, pattern-reconfigurable antennas.

I. INTRODUCTION

Intelligent wireless communication systems have received increasing attention for their applications to many complex communication environments, such as mobile systems and tunnel environments [1]−[4]. In particular, pattern-reconfigurable antennas have been widely applied to

vehicle-to-vehicle (V2V) scenarios. Two kinds of dynamical operating characteristics have been widely used [5], [6]. One is a system with two oppositely directed endfire radiating states. The second is a system with a bidirectional endfire radiating state. Specifically, two switchable endfire radiation states (one toward the front of a vehicle and the other towards its back) can provide message communication links between two vehicles or between a vehicle and access points (APs). On the other hand, the bidirectional endfire state can be used effectively to detect signals from both the front and back of a vehicle or from multiple APs at the same time. An intelligent system can then control the two independent directional operating states to provide message communication links.

Different types of antennas having such versatile radiation characteristics have been reported [5]−[9]. Mechanical or multiport systems are employed in [5], [7], [8] to dynamically control the main beams. This choice makes the antenna system relatively complicated and high cost. In order to make the antenna simple and low-cost, electronically controlled pattern-reconfigurable antennas were reported in [6], [9]. The main beams radiated by them were easily reconfigured using p-i-n (PIN) diodes. Nevertheless, all of the above-mentioned antennas are relatively electrically large in size, i.e., their $ka > 1$, where $k = 2\pi / \lambda_0$ and a is the radius of the smallest sphere that completely encloses the entire antenna system at the operational free-space wavelength λ_0. Consequently, their applications to more compact, smarter, and light-weight communication systems are very limited.

Electrically small antennas (ESAs) have been investigated extensively in recent years. A feature emphasized in these efforts has been the desire to enhance their radiation characteristics, e.g., to increase their directivity. Highly directive ESAs would be advantageous for many 5G (fifth generation and IoT (internet-of-things) applications. A very productive approach to achieve higher directivities has been to combine electric and magnetic radiators to achieve Huygens dipole antennas (HDAs). While mostly electrically large in size, the magneto-electric antennas [e.g., 10−12] effectively employ this design principle. They achieve high directivities, large front-to-back ratios (FTBRs) and wide beamwidths without the need to load the radiators with additional constructs such as slot structures [13], periodic electromagnetic band gap structures [14], or reflector elements [15]. Those additional constructs

significantly increase the overall size and profile of the antenna system. On the other hand, electrically small HDAs have been developed by organically combining metamaterial-inspired electrically small electric and magnetic elements [16]−[26]. They include passive versions such as the single port [16]−[20] and dual port [21]−[23] linearly (LP) and circularly (CP) polarized systems. Active HDA versions include pattern and polarization reconfigurable systems [24], [25] and non-Foster-based broader bandwidth systems [26]. In view of the electrically small sizes and high directivities of these electrically small, multi-functional HDAs, it is expected that they could be even more useful if their versatilities were expanded. In particular, if they could switch between both unidirectional endfire and bidirectional endfire states, they would meet the demands of the noted complex V2V communication ecosystems.

In this paper, an ultra-low-profile, electrically small, pattern-reconfigurable metamaterial-inspired HDA is presented that operates near 1.5 GHz. This operating frequency was selected for the design only to simplify the fabrication of the antenna's prototype and to match our available measurement equipment. The design can be readily adjusted to a different frequency of interest. Its near field resonant parasitic (NFRP) elements include rectangular versions of the electrical Egyptian axe dipoles (EADs) and the magnetic capacitively loaded loops (CLLs). Its reconfigurable driven elements are specially designed in order that the system is pattern-reconfigurable without any modifications to those NFRP elements. Two PIN diodes are utilized to change the current pathways on the driven elements. This arrangement in turn leads to three switchable beam states, i.e., two unidirectional endfire states and one bidirectional endfire state within an overlapping frequency range. In Section II, the antenna configuration is described and its reconfigurable driven element is detailed. A prototype of this design was fabricated and measured; details are presented next in Section III. The measured results are in good agreement with their simulated values. To understand the design principles more completely, the physical mechanisms that lead to its reconfigurable states are detailed. Finally, some conclusions are drawn in Section IV.

II. Pattern-Reconfigurable Metamaterial-Inspired HDA Design

A. Configuration

The configuration of the ultra-low-profile (i.e., ultra-thin), pattern-reconfigurable metamaterial-inspired Huygens dipole ESA is shown in Fig. 1. The corresponding optimized design parameters are given in Table I. The antenna was fabricated using printed circuit board technology.

Fig. 1(a) illustrates that the antenna consists of only one substrate layer. The Rogers Duroid 5880 copper-cladded teflon substrate was selected for the design. It has a relative dielectric constant ε_r = 2.2 and loss tangent tan δ = 0.0009. The substrate was 0.508 mm thick, and the radiation and driven elements were etched into its 0.5 oz (0.017 mm thick) copper layers on both of its sides. The overall shape of the substrate is a disk whose radius is 31 mm.

As shown in Fig. 1(b), two rectangular EAD elements are placed symmetrically with respect to the center of the disk on the upper surface of the substrate. These electric NFRP elements are resonators that are variations of the I-shaped inclusions that constitute the ENG (epsilon-negative) metamaterial unit cells reported in [27]−[29]. The main body of the two EAD elements consists of two long straight copper strips oriented parallel to the x-axis. They have the same width (W4), but have different lengths (L4 ≠ L5). Two pairs of copper strips with the equal lengths (L6) are attached orthogonal to and are centered on these long copper strips along the y-axis. Moreover, eight small copper strips with the equal lengths (L7) extend along the x-axis from the ends of those pairs. The distance between the adjacent edges of the main bodies of these two EAD elements is L8. These two EAD elements separately produce the LP field of an electrical dipole oriented along the x-axis.
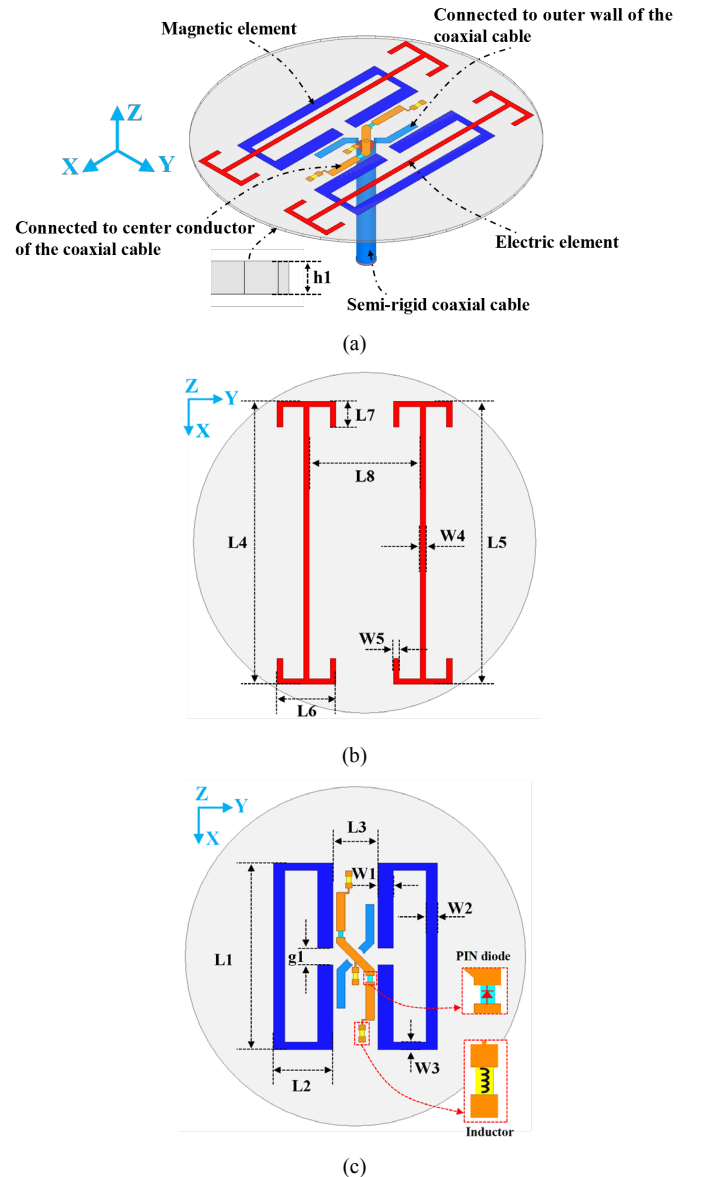

(a)

(b)

(c)

Fig. 1 Configuration of the ultra-low-profile, electrically small, pattern-reconfigurable metamaterial-inspired HDA. (a) 3-D isometric view. (b) Front view. (c) Back view.

As shown in Figs. 1(a) and 1(c), the magnetic elements are two CLLs that have been commonly employed as the inclusions of a MNG (mu-negative) metamaterial unit cell [30]−[33]. They are etched on the lower surface of the substrate. As shown in Fig. 1(c), the two CLLs have the same dimensions and are symmetrically located with respect to the *x*-axis. Each CLL element consists of five copper strips with different widths (*W1, W2,* and *W3*). One longer copper strip is oriented along the *x*-axis and is *L1×W2* in size. Two shorter copper strips are both *L1×W1* in size separated by a gap (*g1*). These two copper strips are connected by a pair of copper strips oriented along the *y*-axis, each with length *L2* and width *W3*. The distance between these two CLL elements is *L3*. In general, these two CLLs elements can separately produce the LP field of a magnetic dipole oriented along the *z*-axis.

These two pairs of CLLs and EADs operate as NFRP elements excited by the driven element. It consists of two isolated copper strips etched halfway between the two CLL elements on the lower surface of the substrate. A KTG 141–50 type, semi-rigid, 50 Ω coaxial cable was selected to feed the driven element. This 50-Ω coaxial feed cable is connected and oriented perpendicular to it. As depicted in Fig. 1(a), its center and external conductors are connected (soldered), respectively, to the two strips of the driven element.

TABLE I.
OPTIMIZED DESIGN PARAMETERS OF THE LOW-PROFILE, ELECTRICALLY SMALL, PATTERN-RECONFIGURABLE METAMATERIAL- INSPIRED HUYGENS DIPOLE ANTENNA (IN MILLIMETERS)

h1 = 0.508	L1 = 34.0	L2 = 10.85	L3 = 8.2	L4 = 51.8
L5 = 51.4	L6 = 10.7	L7 = 4.65	L8 = 20.9	L9 = 7.1
L10 = 7.0	L11 = 1.1	L12 = 8.33	L13 = 2.69	L14 = 1.2
W1 = 2.75	W2 = 2.1	W3 = 1.3	W4 = 0.2	W5 = 1.0
W6 = 1.5	g1 = 3.0	Null		

B. Reconfigurable Driven Element Design

In order to realize the pattern reconfigurability between the two unidirectional endfire states and a bidirectional endfire state, a reconfigurable driven element was specially engineered. It is shown in Fig. 2. Its reconfigurable strip is highlighted in orange; it is connected to the center conductor of the coax feedline. Its passive strip is highlighted in blue; it is connected to the coax's outer conductor. While the 50 Ω coaxial cable is not explicitly displayed, the curved edges of the passive strip at the center of the substrate are connected to the cable's outer conductor. In the center of the disk, the orange and blue strips are crossed through the center of the disk along the ± 45° directions. Recall that they lie in the middle of the two CLLs elements. Their total lengths are not the same along the +45° and -45° directions, i.e., *L12 ≠ 2×L13*. Two copper strips with equal lengths (*L9*) extend from the center diagonal blue strips and are oriented along the ±*x*-axis. Two wedge-shaped strips extend from the center diagonal orange strip along the ± *x*-axis with the same edge length (*L11*). They facilitate easy connectivity to the two additional rectangular copper strips, each *L10×W6* in size, printed along the ± *x*-axis. Furthermore, there are three pairs of square copper patches (*L14×L14*) that

serve as the connection points for three 51 nH coil inductors (LQW18A from Murata). These chokes isolate the dc feed lines required to control the states of the two diodes from any RF signal.
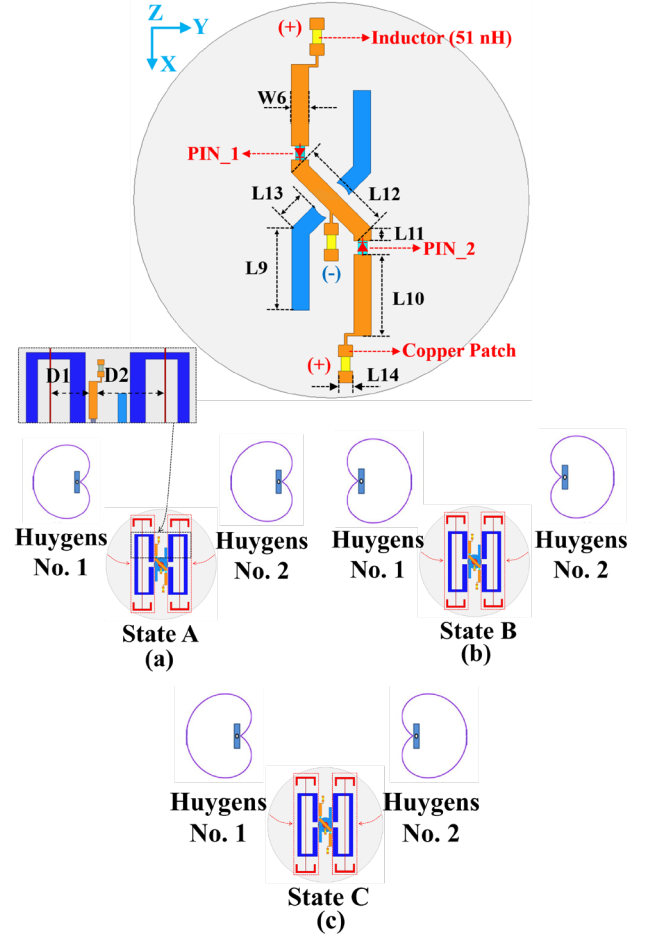

Fig. 2 Locations of the PIN diodes and the RF blocking inductors on the driven element are indicated in the top subplot. The function of the two pairs of magnetic and electric dipoles in each of the three directional states is represented by the cardioid patterns. (a) State A. (b) State B. (c) State C.

As shown in Fig. 2, two PIN diodes (Bar50-02V from Infineon Technologies) were incorporated into the strip connected to the center conductor of the coax. According to the PIN datasheet, each diode acts as a 1.2 Ω resistor in its ON state and a 0.15 pF capacitor in its OFF state [34]. For easy observation, these diodes are denoted as PIN_1 and PIN_2. Their positive poles are connected to the two flat ends of the wedge-shaped copper strips; their negative poles are connected to the straight (orange) strips oriented along the ±*x*-axis. The '+' and '-' labels represent the points at which the DC feed line is connected to the driven element.

Three dynamic states of the system are controlled by the ON-OFF switch operations of the two PIN diodes as illustrated in Fig. 2. The control of these three directional states is determined by the states of the PIN diodes. These operational states are summarized in Table II.

When PIN_1 is turned ON and PIN_2 is turned OFF, the driven element on the - y-axis side of center directly drives the magnetic dipole on the left side. It in turn excites the electric dipole on this side [17]. This in-phase pair generates a Huygens source radiation pattern whose main beam direction is pointed along the -y-axis. Because they are also resonant at the same frequency, the other "passive" pair of magnetic and electric dipoles is also excited. In fact, the currents of this right pair are essentially in the same directions as the left pair. This behavior arises because the distances between the left driven strip and the left and right pairs are very small. These distances, D1 and D2, are illustrated in the inset associated with Fig. 2(a). They are D1 = 7.0 mm (0.035 λ_0) and D2 = 12.4 mm (0.062 λ_0). Thus, the difference between them is quite small, only 0.027 λ_0. Consequently, the phase difference between them is negligible. As a result, the right pair also forms a Huygens source whose main beam direction is pointed along the -y-axis, thus enhancing the gain in that direction. This operational mode is illustrated in Fig. 2(a) and is denoted as State A.

On the other hand, when PIN_1 is turned OFF and PIN_2 is turned ON, the driven element on the +y-axis side of center directly drives the magnetic dipole on the right side, which in turn excites the right-side electric dipole. This pair generates a Huygens source radiation pattern whose main beam is now directed along the +y-axis and whose gain level is reinforced by the Huygens source pair on the left side. This mode is shown in Fig. 2(b) and is denoted as State B.

Finally, when both PIN_1 and PIN_2 are switched ON, both magnetic dipoles are excited with the same phase. The corresponding electric dipoles are then in phase with their respective magnetic dipoles. As a result, two oppositely pointed Huygens sources are created. This bi-directional Huygens radiation state is shown in Fig. 2(c) and is denoted as State C. It is noted that the small difference in the lengths of the EAD elements compensates for the presence of the negative bias pad and, hence, facilitates the equivalent left and right pointing unidirectional Huygens and the bi-directional patterns.

TABLE II
PIN DIODE STATES THAT ATTAIN THE THREE RADIATION PATTERN STATES

Category	State	PIN_1	PIN_2
Fig. 2(a)	A	ON	OFF
Fig. 2(b)	B	OFF	ON
Fig. 2(c)	C	ON	ON

III. SIMULATED AND MEASURED RESULTS

All of the numerical simulations and optimizations of the designs were accomplished with the commercial software ANSYS/Ansoft HFSS, version 18. Realistic material properties for all components were incorporated into these numerical models. A prototype was tested to confirm the predicted three reconfigurable states and their performance characteristics.

A. Results and Performance

The optimized design was fabricated, assembled, and measured. Photographs of the prototype are shown in Fig. 3(a)

and (b). Because the balanced driven element was directly connected to the unbalanced 50 Ω coaxial cable, a 49.5 mm-long sleeve balun (~0.25 λ_0) was employed in the measurement process. This balun is shown in Fig. 3(a). It mitigates any spurious currents induced on the outer walls of the long coax cable and, hence, ensured the accuracy of the measurements of the impedance matching and the far-field directivity pattern characteristics [35], [36]. Because the balun was only ancillary to the measurement, it was not included in the calculation of the *ka* value of the system.

Three different dc bias lines were used to switch the diodes between their ON and OFF states. They are shown in Fig. 3(b). The $|S_{11}|$ values (reflection coefficients) of the antenna in its three operational states as functions of the source frequency were measured with an Agilent E8361A PNA Vector Network Analyzer (VNA). The far-field realized gain patterns and radiation efficiency (RE) were measured with an SG128 multi-probe antenna measurement system at the China Academy of Information and Communications Technology, Chongqing, China [37]. The antenna under test (AUT) in the measurement chamber is shown in Fig. 3(c) along with the ATTEN TPR3003T-3C regulated dc power supply that provided the requisite ~1.4 V to turn on the PIN diodes.
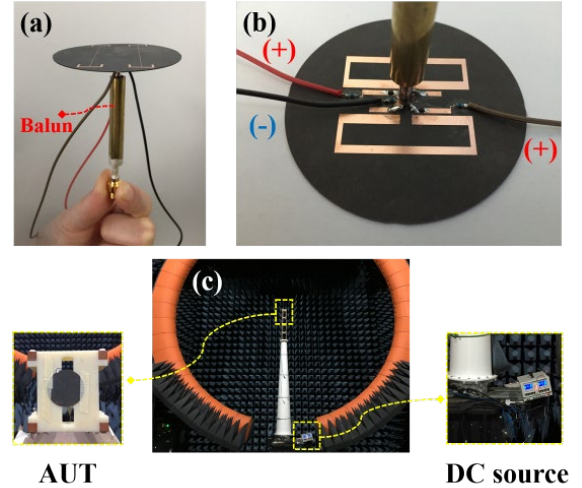

Fig. 3 Fabricated prototype of the ultra-low-profile, electrically small, pattern-reconfigurable metamaterial-inspired HDA. (a) Side view of the assembled antenna. (b) Bottom view of the assembled antenna. (c) The AUT in the multi-probe anechoic chamber.

The measured $|S_{11}|$ results for States A-C, together with their simulated values (taking into account of the presence of the balun), are presented in Fig. 4. The simulated (measured) resonant frequencies for States A-C are 1.511 (1.51) GHz, 1.511 (1.51) GHz, and 1.516 (1.515) GHz, respectively, where $|S_{11}|_{min}$ = -15.1 (-14.6) dB, -15.2 (-15.6) dB, and -16.7 (-16.4) dB. The measured -10 dB bandwidths are 36 MHz (1.50−1.536 GHz, 2.38%), 32 MHz (1.498−1.53 GHz, 2.11%), and 20 MHz (1.505−1.525 GHz, 1.32%), respectively. Thus, the measured overlapped operating bandwidth for States A-C is 20 MHz, covering 1.505–1.525 GHz. The corresponding simulated (measured) electrical size and total height of the system at the resonant frequency $f_{0, sim}$ = 1.511 GHz ($f_{0, meas}$ = 1.51 GHz) were

$ka = 0.98\ (0.98)$ and $0.0026\ \lambda_0\ (0.0026\ \lambda_0)$, respectively. These measured results are in good agreement with their simulated values, confirming that the prototype is indeed electrically small and ultra-low-profile.
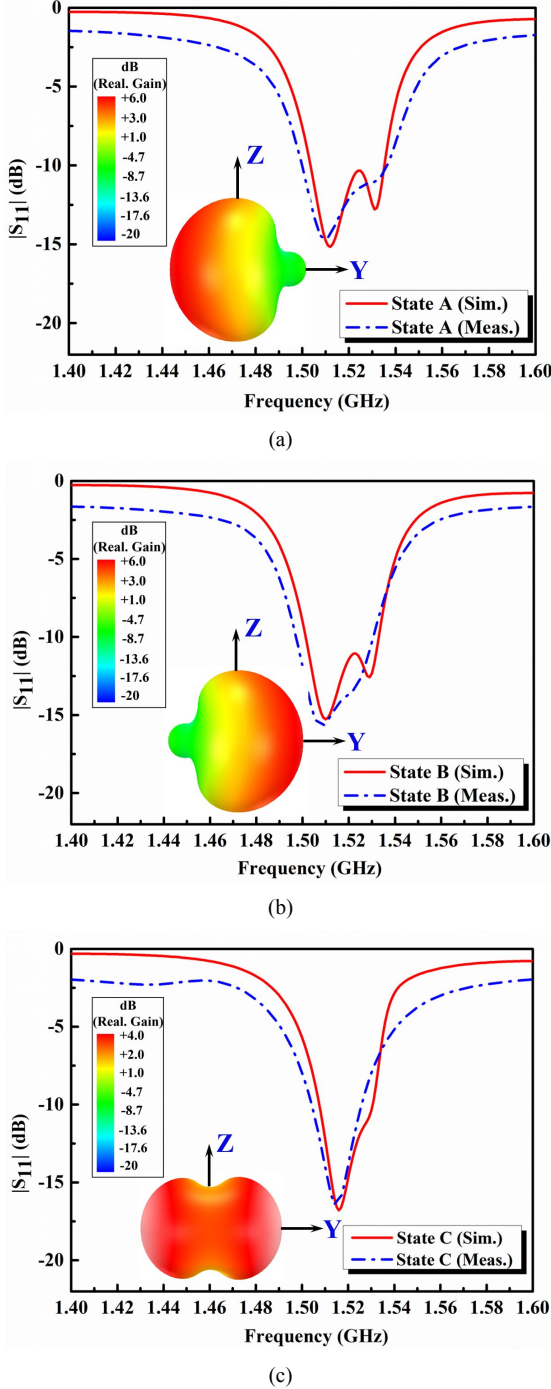

(a)

(b)

(c)

Fig. 4 Simulated and measured $|S_{11}|$ values of the ultra-low-profile, pattern-reconfigurable metamaterial-inspired Huygens dipole ESA in its three directional states as functions of the source frequency. (a) State A. (b) State B. (c) State C.

The simulated and measured realized gain patterns are presented in Fig. 5 at the three resonance frequencies corresponding to the three end-fire radiation states. When the states of the PIN diodes are changed, the main beam direction

of the antenna is redirected as expected. The realized gain patterns of the two unidirectional endfire states, i.e., State A and State B, are shown in Figs. 5(a) and 5(b), respectively. The realized gain patterns of the bidirectional endfire state, i.e., State C, are shown in Fig. 5(c).

In State A, the antenna generated a Huygens source radiation pattern whose maximum is directed along the -y-axis, i.e., along -90°. The simulated (measured) peak realized gain, FTBR, and RE values are 5.59 (5.4) dBi, 14.3 (13.3) dB, and 87.5% (85%), respectively. The 3 dB beam coverage was 94°, from -43° to -137° (102°, from -39° to -141°) in the E-plane (x0y plane) and 120°, from -30° to -150° (111°, from -36° to -147°) in the H-plane (z0y plane). In State B, the antenna generated a Huygens source radiation pattern whose maximum is directed along the +y-axis, i.e., along +90°. The corresponding values for State B are 5.43 (5.4) dBi, 15 (13.3) dB, and 87.7% (85%), respectively. The 3 dB beam coverage was 95°, from 42° to 137° (102°, from 39° to 141°) in the E-plane (x0y plane) and 124°, from 28° to 152° (112°, from 32° to 144°) in the H-plane (z0y plane).
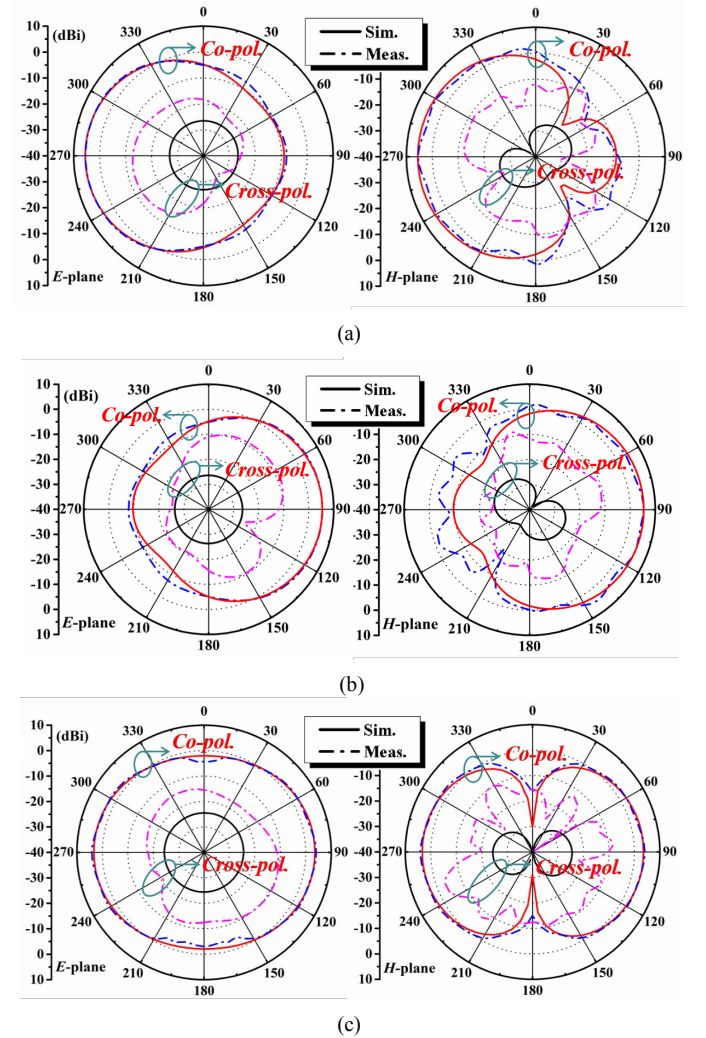

(a)

(b)

(c)

Fig. 5 Simulated and measured realized gain patterns for the three directional states at the simulated (measured) resonance frequencies in their overlapping frequency bands. (a) State A at 1.511 (1.51) GHz. (b) State B at 1.511 (1.51) GHz. (c) State C at 1.516 (1.515) GHz.

In State C, the system generated a bidirectional radiation performance, i.e., a combination of two oppositely directed Huygens source radiation patterns. The simulated (measured) peak realized gain and RE values in the two opposite directions are, respectively, 3.6 dBi and 87.4% at -90° and 3.55 dBi, and 87% at +90°. The 3 dB beam coverage about the -y-axis was 102°, from -39° to -141° (100°, from -39° to -139°) in the E-plane (*x0y* plane) and 92°, from -44° to -136° (101°, from -39° to -140°) in the H-plane (*z0y* plane). Similarly, the 3 dB beam coverage about the +y-axis was 101°, from 40° to 141° (102°, from 39° to 141°) in the E-plane (*z0x* plane) and 93°, from 43° to 136° (101°, from 39° to 151°) in the H-plane (*z0y* plane). The cross-polarization levels in both directions are below -15.3 dB.

The measured and simulated values of the prototype in both states are summarized in Table III for easy comparisons. It is noted that the simulated and measured RE values were higher than 80% in all three directional states. The reason that there are only small differences in the RE values when the diodes are in their ON and OFF states is the fact that they are integrated only on the driven structure and not on the magnetic and electrical NFRP elements, which play the main role in the antenna radiation processes [25]. All of the measured results are generally in good agreement with their simulated values. The relatively small differences are due to fabrication and assembly tolerances.

State	A	B	C
Res. Frequency (GHz)	1.511	1.511	1.516
	1.51	1.51	1.515
Bandwidth (%)	2.1	2.1	1.45
	2.38	2.11	1.32
Peak Realized gain (dBi)	5.59	5.43	3.6
	5.4	5.4	3.55
FTBR (dB)	14.3	15	-
	13.3	13.3	-
RE (%)	87.5	87.7	87.4
	85	85	87
3-dB beam coverage in E-plane	-43°~ -137°	42°~ 137°	-39°~ -141° 40°~141°
	-39°~ -141°	39°~ 141°	-39°~ -139° 39°~ 141°
3-dB beam coverage in H-plane	-30°~ -150°	28°~ 152°	-44°~ -136° 43°~ 136°
	-36°~ -147°	32°~ 144°	-39°~ -140° 39°~ 151°

B. Parameter Studies

Guidelines for the design of electrically small HDAs have been detailed previously in [17]. Consequently, we have elected not to repeat them here. Rather, we emphasize the parameter studies of this ultra-thin design.

The HDA's operational performance characteristics were optimized by changing the electric and magnetic NFRP element's dimensions, the distance between them, and the size of the driven element. Because the magnetic NFRP elements are closer to the driven dipole, they are more strongly coupled to it than the electric ones are. On the other hand, the electric NFRP elements are in close proximity to the magnetic ones and, hence, have a strong capacitive coupling to them. Consequently, their dimensions have a strong influence on the performance characteristics and must be tuned accordingly.

To illustrate these issues, we share some parameter studies that have guided the design and our optimization of the reported pattern-reconfigurable Huygens dipole ESA. The results were obtained by varying one design parameter while keeping all others fixed. Figs. 6 and 7 present the effect of the lengths of the magnetic dipole (L1) and the electric dipole (L4) on the reflection coefficient, and realized gain and FTBR values in State A. On the one hand, as shown in Fig. 6, the change of L1 greatly influences the operating frequency. This confirms that the magnetic dipole size plays an important role in determining it. Similarly, the realized gain and FTBR values witness corresponding changes. On the other hand, when L4 is changed, the radiation performance characteristics (i.e., realized gain and FTBR values) are significantly influenced, but leave the operational bandwidth essentially unchanged, as illustrated in Fig. 7.

(a)

(b)

Fig. 6 The effects on the performance characteristics of the ultra-low-profile, pattern-reconfigurable metamaterial-inspired Huygens dipole associated with changing the magnetic dipole length L1. (a) The reflection coefficient ($|S_{11}|$) values. (b) The realized gain and FTBR values.
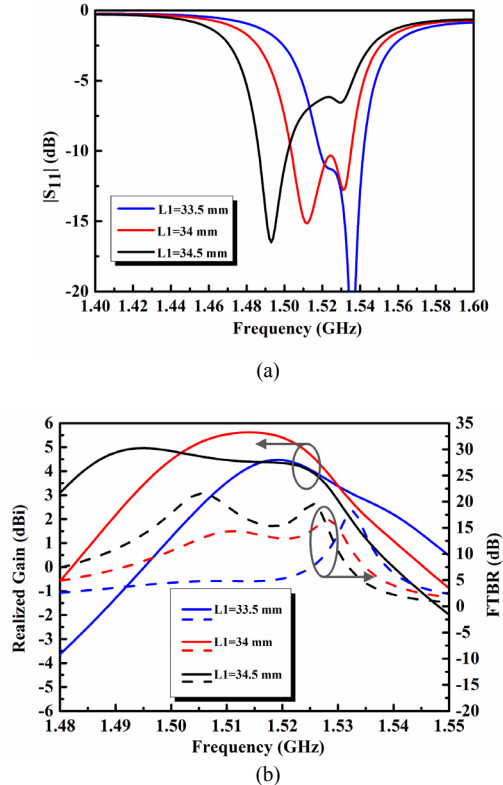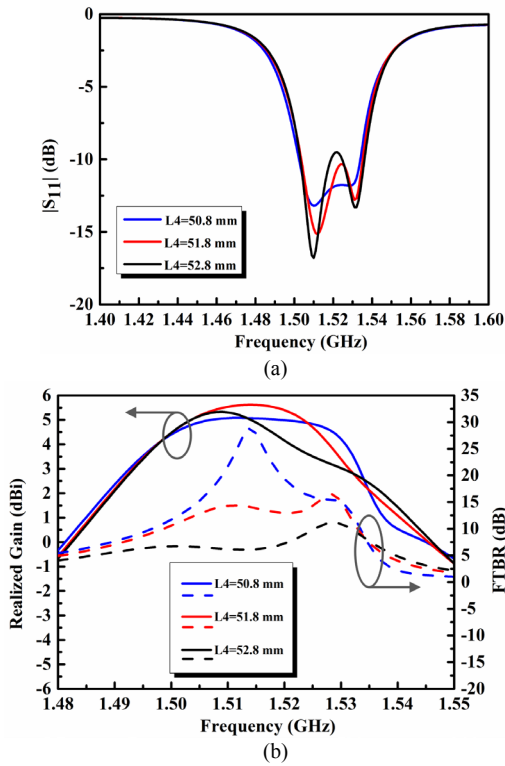
Fig. 7 The effects on the performance characteristics of the ultra-low-profile, pattern-reconfigurable metamaterial-inspired Huygens dipole associated with changing the electric dipole length L4. (a) The reflection coefficient ($|S_{11}|$) values. (b) The realized gain and FTBR values.

C. Operating mechanisms

Note that the simulated maximum realized gain values of the antenna system in State A and State B were 5.59 and 5.43 dBi, respectively. Both values are significantly higher than the theoretical maximum value for an electrically small Huygens source, i.e., $2 \times 1.5 \sim 4.77$ dBi [17, 38]. It was indicated above that the opposite, second pair of magnetic and electric NFRP elements contributed to this enhancement. In order to explain this outcome further, the current distributions on the NFRP and driven elements were investigated.

The surface current distributions on the main copper surfaces, i.e., the upper surface of the driven element and the upper surfaces of the NFRP elements, are depicted in Fig. 8. They are presented at the times: t = 0, T/4, T/2 and 3T/4, corresponding to the period T associated with the selected frequency point within the simulated bandwidth of State A, 1.525 GHz, that is centered between the two resonance dips in Fig. 4(a). For easier observation, the current directions are highlighted with the additional red (for the left CLL and EAD NFRP pair) and blue (for the right CLL and EAD NFRP pair) solid arrows.

It is clear that since PIN_1 is ON and PIN_2 is OFF, only the left portion of the driven element is operating. Thus, it induces the majority of the surface currents distributed on the left CLL and EAD pair. Referring to the current behavior analysis of the Huygens dipole ESA reported in [17], the variation of the red arrows on the left CLL and EAD NFRP pair over the entire period indicates that they are resonant and in-phase. The

indicated current directions of this combination point to its generation of an unidirectional Huygens cardioid radiation pattern whose maximum is directed along the -*y*-axis [17, 38]. This feature is illustrated in the left-most subplot of Fig. 9.
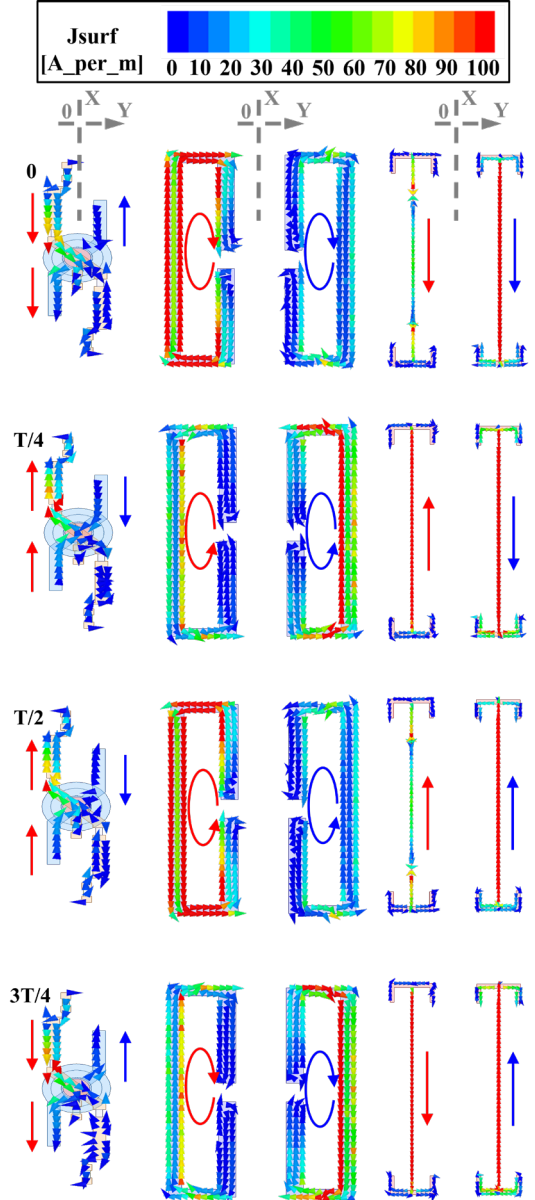

Fig. 8 Surface current distributions on the driven element and on the upper faces of the CLL and EAD NFRP elements at quarter period intervals when the antenna system is in its State A.
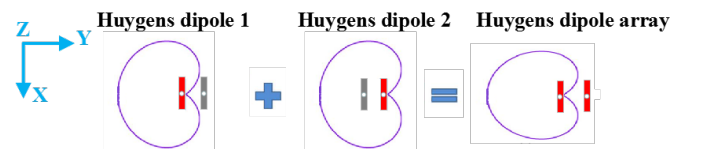

Fig. 9 Design concept of the ultra-low-profile, pattern-reconfigurable Huygens dipole ESA in State A.

Recall from Fig. 1 that the left and right pairs of NFRP elements are in rather close proximity (only separated by 0.1 λ_0). As the blue and red arrows in Fig. 8 highlight, the left driven pair of NFRP elements induces currents on the right pair. Comparing the current directions on the CLL and EAD elements, the phases of the two CLL elements and of the two EAD elements are approximately the same. Moreover, there is the associated 90° phase difference between these magnetic and electric pairs required to produce the Huygens cardioid pattern. These currents illustrate that the Huygens field that the right pair radiates is then pointed in the same direction as the left pair, as illustrated in the middle subplot of Fig. 9. However, it has a lower magnitude because the right pair is indirectly excited and is displaced at a distance "behind" the driven pair. According to two-element array theory [39], the realized gain of the entire antenna in its State A is thus significantly higher than the maximum theoretical value, 4.77 dBi. This composite Huygens field is illustrated in the right-most subplot of Fig. 9.

Fig. 10 Surface current distributions on the driven element and on the upper faces of the CLL and EAD NFRP elements at quarter period intervals when the antenna system is in its State B.

Fig. 11 Design concept of the ultra-low-profile, pattern-reconfigurable Huygens dipole ESA in State B.
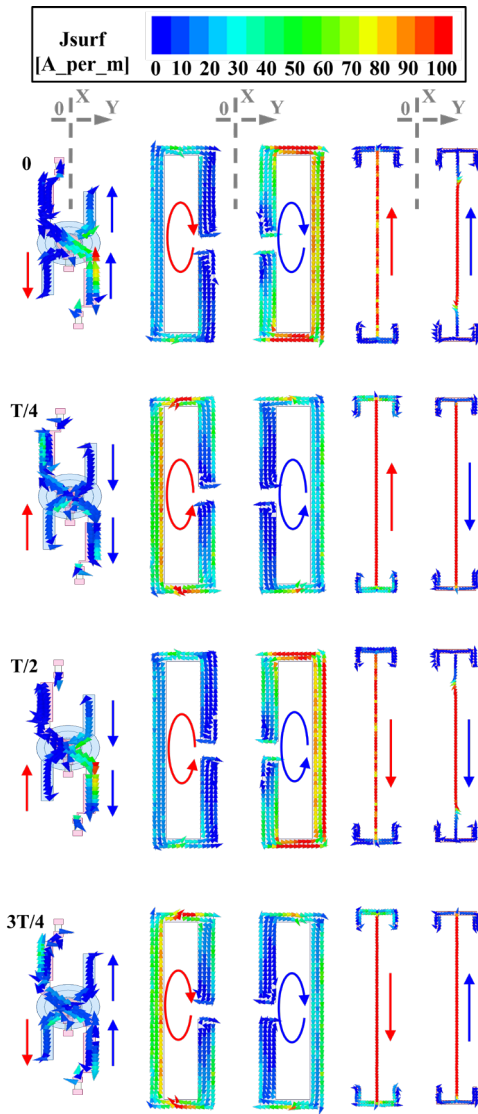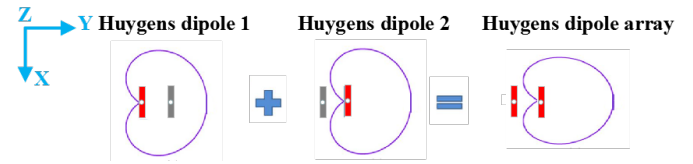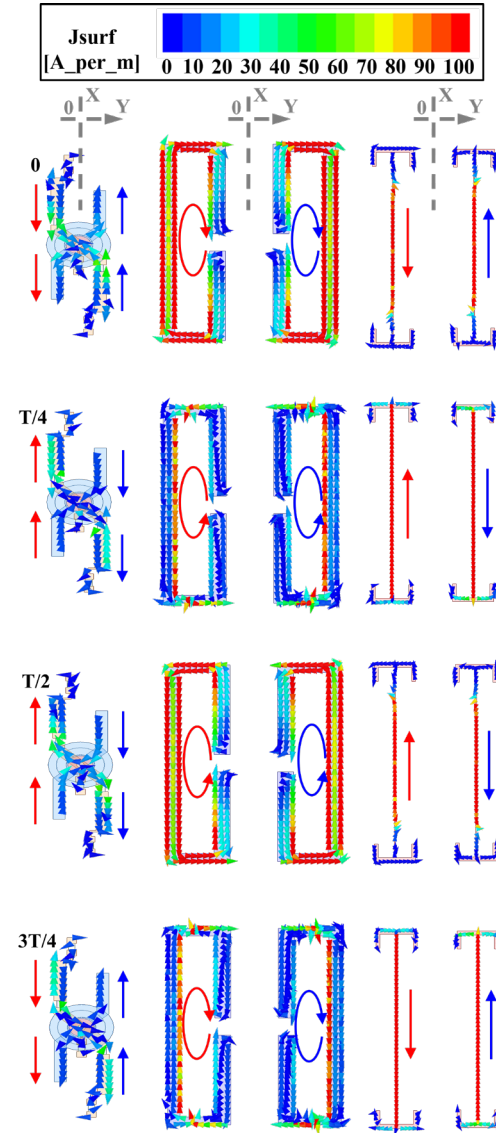

Fig. 12 Surface current distributions on the driven element and on the upper faces of the CLL and EAD NFRP elements at quarter period intervals when the antenna system is in its State C.
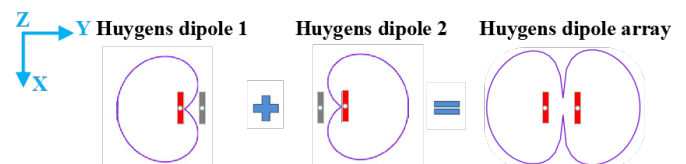

Fig. 13 Design concept of the ultra-low-profile, pattern-reconfigurable Huygens dipole ESA in State C.

TABLE IV
COMPARISON OF THE ULTRA-LOW-PROFILE, ELECTRICALLY SMALL, PATTERN-RECONFIGURABLE METAMATERIAL-INSPIRED HDA WITH
RELATED RECONFIGURABLE ANTENNAS REPORTED IN THE LITERATURE[*]

Ref.	ka	FBW (%)	Peak gain (dBi)	RE (%)	Height	Switch No.	Type of patterns	Configuration
[6]	2.81	11.3	~6.7	~75	$0.06\,\lambda_0$	2	D & B	2-D
[24]	0.94	2.73	3.59	85	$0.05\,\lambda_0$	3	D	3-D
[40]	1.32	15	3.5	83	$0.024\,\lambda_0$	4	D	2-D
[41]	0.6	2.7	8.5	89.8	$0.095\,\lambda_0$	2	D	3-D
[42]	0.94	12.9	4.43	70.5	$0.0007\,\lambda_0$	4	D	2-D
This work	0.98	1.32	5.4	85	$0.0026\,\lambda_0$	2	UD & B	2-D

[*]In the "Type of patterns" column, D, UD or B represents a directional, unidirectional or bidirectional pattern, respectively.
In the "Configuration" column, 2-D or 3-D indicates that the antenna configuration is planar or volumetric, respectively.

When the antenna operates at State C, both pairs of the CLL and EAD NFRP elements are excited directly by the driven element. The current distributions on the upper surface of the elements have the same orientations are those shown in Fig. 8, indicting the left pair radiates into the $-y$ direction as it does in State A. On the other hand, the currents on the right pair of CLL and EAD elements have the same orientations are those shown in Fig. 10, indicating the right pair radiates into the $+y$ direction as it does in State B. Consequently, the two NFRP pairs generate oppositely directed unidirectional Huygens patterns. Their combination yields the desired bidirectional radiation performance. The cardioid patterns radiated by each Huygens pair and the composite bidirectional pattern are illustrated in Fig. 13.

To emphasize that the ultra-low-profile, electrically small, pattern-reconfigurable HDA described herein is simpler, has improved functionalities, and is more compact that other recently reported pattern-reconfigurable antennas, a comprehensive comparison is given in Table IV. To make this comparison fair, the electrical sizes, bandwidths, realized gain values, RE values, height, numbers of diodes employed, type of pattern and configuration performance characteristics are listed.

Two HDAs with pattern-reconfigurability were reported in [24] and [40]. The volumes that those two antennas occupy are, respectively, $4.26\times10^{-3}\,\lambda_0^3$ ($ka = 0.94$) and $4.23\times10^{-3}\,\lambda_0^3$ ($ka = 1.32$). Their peak realized gain values are approximately the same, ~3.5 dBi. The volume of the antenna reported herein is $0.29\times10^{-3}\,\lambda_0^3$, 14.7 times smaller than the one in [24] and 14.6 times smaller than the one in [40]. While the RE values reported herein are approximately the same as those in [24] and [40], the measured peak realized gains in both unidirectional states is significantly higher at 5.4 dBi.

From a practical point-of-view, the design herein achieves two types of pattern-reconfigurable performance in three states with only two PIN diodes in an ultra-low-profile configuration. Two Yagi-Uda, pattern-reconfigurable ESAs were reported in [41] and [42]. Both of those antennas had only one type of pattern-reconfigurable performance that was achieved with two

driven element and on the upper surfaces of the NFRP elements are shown in Fig. 12 when the antenna is operating in this state at 1.525 GHz. The currents on the left pair of CLL and EAD PIN diodes in [41] and four in [42]. A pattern-reconfigurable antenna that achieved two types of pattern-reconfigurable performance with two PIN diodes was reported in [6]. However, it requires a large ground plane and, as a consequence, its electrical size was very large.

It is concluded from the comparisons given in Table IV that the prototype reconfigurable HDA reported herein indeed has an ultra-low profile and a simple design while being compact and versatile. While the bandwidth is expectedly narrow because of its electrically small size, the compactness and multifunctional features are quite attractive for the many existing and aspirational narrowband applications. Moreover, more bandwidth could be realized by introducing non-Foster elements as was achieved in [26].

IV. CONCLUSION

An ultra-low-profile, electrically small, pattern-reconfigurable, metamaterial-inspired Huygens dipole antenna was presented. The pattern-reconfigurability was achieved with an ultra-thin structure, significantly reducing the profile of the previously successful pattern-reconfigurable HDA [24]. The Huygens dipole elements were achieved using NFRP elements derived from metamaterial-inspired unit cell inclusions. The reported multi-functional configuration was achieved through the development of a highly compact and simple reconfigurable driven element implemented with only two PIN diodes. By manipulating their ON / OFF states, the antenna can realize two unidirectional endfire states, each state radiating in opposite directions, as well as a bidirectional endfire state. The principles of operation of this antenna were described. A prototype was fabricated and tested. The measured results are in good agreement with their simulated values, confirming the design strategy and the final optimized design. The measured overlapped operating fractional bandwidth for the three states is 1.32%, covering 1.505–1.525 GHz. The realized gain values in all three states were stable. The maximum realized gain values

in States A, B, and C were 5.4, 5.4, and 3.55 dBi, respectively. The several advantages of this ultra-low-profile, electrically small, reconfigurable antenna make it attractive for many V2V communication and tunnel environments.

REFERENCES

[1] A. Cidronali, S. Maddio, M. Passafiume, and G. Manes, "Car talk: Technologies for vehicle-to-roadside communications," *IEEE Microw. Mag.*, vol. 17, no. 11, pp. 40–60, Nov. 2016.

[2] F. Liu, Z. J. Zhang, W. H. Chen, Z. H. Feng, and M. F. Iskander, "An endfire beam-switchable antenna array used in vehicular environment," *IEEE Antennas Wireless Propag. Lett.*, vol. 9, pp. 195–198, 2010.

[3] S. Poochaya and P. Uthansakul, "Beam tracking in switched-beam antenna system for V2V communication," *Int. J. Antennas Propag.*, vol. 2016, Art. no. 4169619, Jan. 2016.

[4] Q. Xin, F.-S. Zhang, B.-H. Sun, Y.-L. Zou, and Q.-Z. Liu, "Yagi-Uda antenna with small size for vehicles," *Electron. Lett.*, vol. 47, no. 7, pp. 428–430, 2011.

[5] Y.-Q. Wen, B.-Z. Wang, and X. Ding, "Planar microstrip endfire antenna with multiport feeding," *IEEE Antennas Wireless Propag. Lett.*, vol. 15, pp. 556–559, 2016.

[6] R. Wang, B.-Z. Wang, G.-F. Gao, X. Ding, and Z.-P. Wang, "Low-profile pattern-reconfigurable vertically polarized endfire antenna with magnetic-current radiators," *IEEE Antennas Wirel. Propag. Lett.*, vol.17, pp. 829-832, 2018.

[7] F. Liu, Z. Zhang, W. Chen, Z. Feng, and M. F. Iskander, "An endfire beam-switchable antenna array used in vehicular environment," *IEEE Antennas Wireless Propag. Lett.*, vol. 9, pp. 195–198, 2010.

[8] A. M. Morishita, C. K. Kitamura, A. T. Ohta, and W. A. Shiroma, "A liquid-metal monopole array with tunable frequency, gain, and beam steering," *IEEE Antennas Wireless Propag. Lett.*, vol. 12, pp.1388–1391, 2013.

[9] C.-H. Ko, I.-Y. Tarn, and S.-J. Chung, "A compact dual-band pattern diversity antenna by dual-band reconfigurable frequency-selective reflectors with a minimum number of switches," *IEEE Trans. Antennas Propag.*, vol. 61, no. 2, pp. 646–654, Feb. 2013.

[10] B. Q. Wu and K.-M. Luk, "A broadband dual-polarized magneto-electric dipole antenna with simple feeds," *IEEE Antennas Wirel. Propag. Lett.*, vol. 8, pp. 60-63, 2009.

[11] K.-M. Luk and B. Wu, "The magnetoelectric dipole—A wideband antenna for base stations in mobile communications," *Proc. IEEE*, vol. 100, no. 7, pp. 2297-2307, Jul 2012.

[12] C. Ding and K.-M. Luk, "Low-profile magneto-electric dipole antenna," *IEEE Antennas Wirel. Propag. Lett.*, vol. 15, pp. 1642-1644, 2016.

[13] M.-C. Tang and R. W. Ziolkowski, "Efficient, high directivity, large front-to-back-ratio, electrically small, near-field-resonant-parasitic antenna," *IEEE Access*, vol. 1, no. 1, pp. 16 - 28, May 2013.

[14] P. Jin and R. W. Ziolkowski, "High directivity, electrically small, low-profile, near-field resonant parasitic antennas," *IEEE Antennas Wireless Propag. Lett.*, vol. 11, pp. 305-309, 2012.

[15] S. Lim and H. Ling, "Design of electrically small Yagi antenna," *Electron. Lett.*, vol. 43, no. 5, pp. 3–4, Mar. 2007.

[16] R. W. Ziolkowski, "Low profile, broadside radiating, electrically small Huygens source antennas," *IEEE Access*, vol. 3, pp. 2644-2651, Dec. 2015.

[17] M.-C. Tang, H. Wang, and R. W. Ziolkowski, "Design and testing of simple, electrically small, low-profile, Huygens source antennas with broadside radiation performance," *IEEE Trans. Antennas Propag.*, vol. 64, no. 11, pp. 4607-4617, Nov. 2016.

[18] M.-C. Tang, T. Shi, and R. W. Ziolkowski, "A study of 28 GHz, planar, multi-layered, electrically small, broadside radiating, Huygens source antennas," *IEEE Trans. Antennas Propag.*, vol. 65, no. 12, pp. 6345-6354, Dec. 2017.

[19] W. Lin and R. W. Ziolkowski, "Electrically-small, low-profile, Huygens circularly polarized antenna," *IEEE Trans. Antennas Propag.*, vol. 66, no. 2, pp. 636-643, Feb. 2018.

[20] M.-C. Tang, Z. Wu, T. Shi, and R. W. Ziolkowski, "Dual-band, linearly polarized, electrically small Huygens dipole antennas," *IEEE Trans. Antennas Propag.*, vol. 67, no. 1, pp. 37-47, Jan. 2019.

[21] P. Alitalo, A. O. Karilainen, T. Niemi, C. R. Simovski, and S. A. Tretyakov, "Design and realisation of an electrically small Huygens source for circular polarisation," *IET Microw. Antennas Propag.*, vol. 5, no. 7, pp. 783–789, 2010.

[22] T. Niemi, P. Alitalo, A. O. Karilainen, and S. A. Tretyakov, "Electrically small Huygens source antenna for linear polarisation," *IET Microw. Antennas Propag.*, vol. 6, no. 7, pp. 735–739, 2012.

[23] M.-C. Tang, Z. Wu, T. Shi, H. Zeng, W. Lin, and R. W. Ziolkowski, "Dual-linearly polarized, electrically small, low-profile, broadside radiating, huygens dipole antenna," *IEEE Trans. Antennas Propag.*, vol. 66, no. 8, pp. 3877–3885, Aug. 2018.

[24] M.-C. Tang, B. Zhou, and R. W. Ziolkowski, "Low-profile, electrically small, Huygens source antenna with pattern-reconfigurability that covers the entire azimuthal plane," *IEEE Trans. Antennas Propag.*, vol. 65, no. 3, pp. 1063-1072, Mar. 2017.

[25] M.-C. Tang, Z. Wu, T. Shi, and R. W. Ziolkowski, "Electrically small, low-profile, planar, Huygens dipole antenna with quad-polarization diversity," *IEEE Trans. Antennas Propag.*, vol. 66, no. 12, pp. 6772-6780, Dec. 2018.

[26] M.-C. Tang, T. Shi, and R. W. Ziolkowski, "Electrically small, broadside radiating Huygens source antenna augmented with internal non-Foster elements to increase its bandwidth," *IEEE Antennas Wirel. Propag. Lett.*, vol.16, pp. 712-715, 2017.

[27] R. W. Ziolkowski, "Design, fabrication, and testing of double negative metamaterials," *IEEE Trans. Antennas Propagat.*, vol. 51, no. 7, pp. 1516-1529, July 2003.

[28] W. Cao, B. Zhang, A. Liu, T. Yu, D. Guo, and Y. Wei, "Broadband high gain periodic endfire antenna by using I-shaped resonator (ISR) structures," *IEEE Antennas Wireless Propag. Lett.*, vol. 11, pp. 1470–1473, 2012.

[29] Y. H. Sun, G. J. Wen, H. Y. Jin, P. Wang, and Y. J. Huang, "Gain enhancement for wide bandwidth endfire antenna with I-shaped resonator (ISR) structures," *Electron. Lett.*, vol. 49, no. 12, pp. 736–737, 2013.

[30] A. Erentok, P. Luljak, and R. W. Ziolkowski, "Antenna performance near a volumetric metamaterial realization of an artificial magnetic conductor," *IEEE Trans. Antennas and Propagat.*, vol. 53, no. 1, pp. 160-172, Jan. 2005.

[31] J. D. Baena, J. Bonache, F. Martín, R. M. Sillero, F. Falcone, T. Lopetegi, M. A. G. Laso, J. G.-García, I. Gil, M. F. Portillo, and M. Sorolla, "Equivalent-circuit models for split-ring resonators and complementary split-ring resonators coupled to planar transmission lines," *IEEE Trans. Microw. Theory Tech.*, vol. 53, no. 4, pp. 1451-1461, Apr. 2005.

[32] A. Erentok, R. W. Ziolkowski, J. A. Nielsen, R. B. Greegor, C. G. Parazzoli, M. H. Tanielian, S. A. Cummer, B.-I. Popa, T. Hand, D. C. Vier and S. Schultz, "Low frequency lumped element-based negative index metamaterial," *Appl. Phys. Lett.*, vol. 91, 184104, 02 Nov. 2007.

[33] A. Erentok, R. W. Ziolkowski, J. A. Nielsen, R. B. Greegor, C. G. Parazzoli, M. H. Tanielian, S. A. Cummer, B.-I. Popa, T. Hand, D. C. Vier and S. Schultz, "Lumped element-based, highly sub-wavelength negative index metamaterials at UHF Frequencies," *J. Appl. Phys.*, vol. 104, no. 3, 034901, Aug. 2008.

[34] Bar50-02V from Infineon Technologies. [Online]. Available: https://www.infineon.com/dgdl/Infineon-BAR50SERIES-DS-v01_01-en.pdf?fileId=db3a304314dca3890114fea7dd410a92.

[35] S. A. Saario, J. W. Lu, and D. V. Thiel, "Full-wave analysis of choking characteristics of sleeve balun on coaxial cables," *Electron. Lett.*, vol. 38, no. 7, pp. 304–305, Mar. 2002.

[36] C. Icheln, J. Krogerus, and P.Vainikainen, "Use of balun chokes in small-antenna radiation measurements," *IEEE Trans. Antennas Propag.*, vol.53, no. 2, pp. 498-506, Apr. 2004.

[37] SG128 multi-probe antenna measurement system. [Online]. Available: https://www.mvg-world.com/en/system/files/datasheet_sg128_bd.pdf.

[38] A. D. Yaghjian, "Increasing the supergain of electrically small antennas using metamaterials," *in Proc. EuCAP*, Apr. 2009, pp. 858–860.

[39] C. A. Balanis, *Antenna Theory: Analysis and Design*. New York, NY, USA: Wiley, 2005

[40] J. Ouyang, Y. M. Pan, and S. Y. Zheng, "Center-fed unilateral and pattern reconfigurable planar antennas with slotted ground plane," *IEEE Trans. Antennas Propag.*, vol. 66, no. 10, pp. 5139-5149, Oct. 2018.

[41] S. Lim and H. Ling, "Design of electrically small, pattern reconfigurable Yagi antenna," *Electron. Lett.*, vol. 43, no. 24, pp. 1326–1327, Nov. 2007.

[42] M.-C. Tang, B. Zhou, Y. Duan, X. Chen, and R. W. Ziolkowski, "Pattern-reconfigurable, flexible, wideband, directive, electrically small near-field resonant parasitic antenna," *IEEE Trans. Antennas Propag.*, vol. 66, no. 5, pp. 2271-2280, May 2018.

Zhentian Wu was born in Hefei, China, in 1994. He received the B.S. degree from the West Anhui University, Luan, China, in 2016. He is currently pursuing the ph. D degree in electronics and communication engineering in the School of Microelectronics Communication Engineering, Chongqing University, China.

He current research interests include electrically small antenna and directional antenna and their applications.
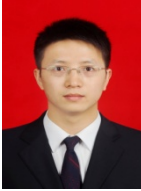
Ming-Chun Tang (S'12–M'13–SM'16) received the B. S. degree in physics from the Neijiang Normal University, Neijiang, China, in 2005 and the Ph. D. degree in radio physics from the University of Electronic Science and Technology of China (UESTC), in 2013. From August 2011 to August 2012, he was also with the Department of Electrical and Computer Engineering, The University of Arizona, Tucson, AZ, USA, as a Visiting Scholar. He is currently a Professor in the School of Microelectronics and Communication Engineering, Chongqing University, China. His research interests include electrically small antennas, RF circuits, metamaterial designs and their applications.

Prof. Tang was a recipient of the Best Student Paper Award in the 2010 International Symposium on Signals, Systems and Electronics (ISSSE2010) held in Nanjing, China. His Ph.D. student received Best Student Paper Award from the IEEE 7th Asia-Pacific Conference on Antennas and Propagation (2018 IEEE APCAP) held in Auckland, New Zealand. He is the founding Chair of the IEEE AP-S / MTT-S Joint Chongqing Chapter. He serves on the Editorial Boards of several journals, including *IEEE Access, IET Electronics Letters* and *IET Microwaves, Antennas & Propagation*. He has also served on the review boards of many journals, including the *IEEE Transactions on Antennas and Propagation, IEEE Transactions on Microwave Theory and Techniques, IEEE Antennas and Wireless Propagation Letters, IEEE Antennas and Propagation Magazine, IEEE Microwave and Wireless Components Letters*, and many international conferences as a General Chair, TPC Member, Session Organizer, and the Session Chair.

Mei Li (M'16) received the Ph.D. in radio physics from the University of Electronic Science and Technology of China, Chengdu, in 2016. From 2014 to 2016, she was with the Applied Electromagnetics Research Group, University of California at San Diego, San Diego, CA, USA, as a Visiting Graduate. She is currently with Chongqing University. Her current research interests include metasurfaces, antennas and arrays.

Richard W. Ziolkowski received the B.Sc. (magna cum laude) degree (Hons.) in physics from Brown University, Providence, RI, USA, in 1974; the M.S. and Ph.D. degrees in physics from the University of Illinois at Urbana-Champaign, Urbana, IL, USA, in 1975 and 1980, respectively; and the Honorary Doctorate degree from the Technical University of Denmark, Kongens Lyngby, Denmark in 2012.

He became a Professor Emeritus at the University of Arizona in 2018, where he was a Litton Industries John M. Leonis Distinguished Professor in the Department of Electrical and Computer Engineering in the College of Engineering and was also a Professor in the College of Optical Sciences. He was the Computational Electronics and Electromagnetics Thrust Area Leader with the Lawrence Livermore National Laboratory, Engineering Research Division, in Livermore, CA before joining The University of Arizona, Tucson, AZ, USA, in 1990. He is currently a Distinguished Professor in the Global Big Data Technologies Centre in the Faculty of Engineering and Information Technologies (FEIT) at the University of Technology Sydney, Ultimo NSW, Australia. His current research interests include the application of new mathematical and numerical methods to linear and nonlinear problems dealing with the interaction of electromagnetic and acoustic waves with complex linear and nonlinear media, as well as metamaterials, metamaterial-inspired structures, nano-structures, and other classical and quantum applications-specific configurations.

Dr. Ziolkowski became a Fellow of the Optical Society of America in 2006 and the American Physical Society in 2016. He was the recipient of the 2019 IEEE Electromagnetics Award (IEEE Field Award). He was the Australian DSTO Fulbright Distinguished Chair in Advanced Science and Technology from 2014-2015. He was a 2014 Thomas-Reuters Highly Cited Researcher. He served as the President of the IEEE Antennas and Propagation Society in 2005. He is also actively involved with the URSI, OSA and SPIE professional societies.